Received: 19 October 2023 | Revised: 17 January 2024 | Accepted: 22 January 2024

DOI: 10.1002/jbm.a.37682

Society For Biomaterials

WILEY

RESEARCH ARTICLE

3D printing modality effect: Distinct printing outcomes dependent on selective laser sintering (SLS) and melt extrusion

Jeong Hun Park[1,2] | Sarah Jo Tucker[3] | Jeong-Kee Yoon[4] | YongTae Kim[1,5,6] | Scott J. Hollister[1,2]

[1]Wallace H. Coulter Department of Biomedical Engineering, Georgia Institute of Technology and Emory University, Atlanta, Georgia, USA

[2]Center for 3D Medical Fabrication, Georgia Institute of Technology and Emory University, Atlanta, Georgia, USA

[3]Global Center for Medical Innovation, Atlanta, Georgia, USA

[4]Department of Systems Biotechnology, Chung-Ang University, Anseong-si, Gyeonggido, Republic of Korea

[5]George W. Woodruff School of Mechanical Engineering, Georgia Institute of Technology, Atlanta, Georgia, USA

[6]Parker H. Petit Institute for Bioengineering and Bioscience (IBB), Georgia Institute of Technology, Atlanta, Georgia, USA

Correspondence
Jeong Hun Park and Scott J. Hollister, Wallace H. Coulter Department of Biomedical Engineering, Georgia Institute of Technology and Emory University, 313 Ferst Drive, Atlanta, GA 30332, USA.
Email: jeonghun.park@bme.gatech.edu and scott.hollister@bme.gatech.edu

Funding information
National Institutes of Health, Grant/Award Number: R01 HD 086201

Abstract

A direct and comprehensive comparative study on different 3D printing modalities was performed. We employed two representative 3D printing modalities, laser- and extrusion-based, which are currently used to produce patient-specific medical implants for clinical translation, to assess how these two different 3D printing modalities affect printing outcomes. The same solid and porous constructs were created from the same biomaterial, a blend of 96% poly-ε-caprolactone (PCL) and 4% hydroxyapatite (HA), using two different 3D printing modalities. Constructs were analyzed to assess their printing characteristics, including morphological, mechanical, and biological properties. We also performed an in vitro accelerated degradation study to compare their degradation behaviors. Despite the same input material, the 3D constructs created from different 3D printing modalities showed distinct differences in morphology, surface roughness and internal void fraction, which resulted in different mechanical properties and cell responses. In addition, the constructs exhibited different degradation rates depending on the 3D printing modalities. Given that each 3D printing modality has inherent characteristics that impact printing outcomes and ultimately implant performance, understanding the characteristics is crucial in selecting the 3D printing modality to create reliable biomedical implants.

KEYWORDS

3D printing, 3D printing characteristics, melt extrusion 3D printing, poly-ε-caprolactone (PCL), selective laser sintering

1 | INTRODUCTION

Diverse 3D printing modalities based on different printing mechanisms have been applied to numerous biomedical engineering fields including tissue engineering and regenerative medicine. 3D printing has demonstrated great promise with high design flexibility as a fabrication strategy to create patient-specific implants for personalized medicine.[1,2] The external geometry of patient-specific 3D biomedical implants, including outer shape and dimension, is determined based on the patient's anatomic defects. The implant material and inner architecture are also critical factors in designing implants as they influence directly the structural, mechanical, and biological performances of the implant. Those should be determined based on the specific design requirements of the implant including porosity, mechanical strength, degradation behavior, permeability, and cell response.[3–5] It is also important to determine those factors based on the technical features and the capabilities of the 3D printing modality employed to create the implant. Other than the printing orientation effect, resulting from a fundamental principal of the layer-by-layer process, each 3D printing modality exhibits a different printing performance, including printing efficiency, resolution, raw material selectivity, and design flexibility, which are closely related to the intrinsic printing mechanism. Given that printing performance significantly influences the printing outcomes, especially the final quality and performance of the printed implants, understanding and characterizing the features and capabilities of different 3D printing modalities is of paramount importance.

Many studies have investigated the dependence of printing results on printing parameters for a single given printing modality.[6–10] Many literature review studies have also contributed to our understanding of the merits and drawbacks of different 3D printing modalities.[11–13] However, there has been no direct comparison of different 3D printing modalities using the same input material to provide a detailed rationale for choosing the printing modality to produce biomedical implants for a given clinical indication. Deriving a suitable 3D printing modality through a direct comparison of printing outcomes from different printing modalities is therefore required to ensure the reliable printing quality and performance of biomedical implants, especially based on a fixed biomaterial input.

We hypothesized that different 3D printing modalities would yield significantly distinct printing outcomes despite using the same raw biomaterial input. In this regard, an in-depth comparative study on two representative 3D printing modalities for clinical translation of biomedical implants, selective laser sintering (SLS) and melt extrusion modalities, was performed to compare and understand their respective printing outcome characteristics. 3D constructs of the same geometry were printed using one the same raw input biomaterial, a blend of 96% poly-ε-caprolactone (PCL) and 4% hydroxyapatite (HA), using two different printing modalities. Printing outcomes were compared in terms of morphology, mechanical property, and cell responses. In vitro degradation behavior in an alkaline medium was also compared in terms of the changes in the structural, mechanical, and material properties of the 3D constructs printed from the two different 3D printing modalities.

2 | MATERIALS AND METHODS

2.1 | Materials

The raw PCL powder (CAPA 6501, M_w = 50,000, Polysciences, Inc., UK) was cryogenically milled (Jet Pulverizer, Moorestown, NJ, USA) and sieved to an average particle size of 40–60 μm. HA (Plasma Biotal Ltd., UK) with an average particle size of 5 μm was then mixed with the milled PCL powder with a ratio of 4% (wt/wt) for use in both SLS and extrusion 3D printing.

2.2 | 3D constructs design

All 3D constructs were designed using SolidWorks® software. Solid cylindrical constructs of 4.8 mm height with 10 mm and 9.5 mm diameter were designed for SLS and extrusion 3D printing, respectively. A porous cylinder design with a continuous struts (500 600 μm) in a grid pattern, which has been extensively used for extrusion 3D printing, was designed for SLS printing.[12,14] 3D grid pattern of 4.8 mm height and 9.5 mm diameter, without strut width feature, was also designed using Surface Extrude tool to enhance the shape fidelity for extrusion 3D printing of porous cylindrical construct. Solid and hollow rectangular constructs of 20 20 2 mm and 20 10 20 mm were designed for contact angle measurement, respectively. Solid disks with 10 mm diameter and 2 mm thickness were also designed for cell attachment and proliferation tests.

2.3 | 3D printing

SLS-based 3D printing was performed using a Formiga P110 (electro-optical systems [EOS] GmbH, Krailling, Germany). STL files of 3D constructs were imported into a Magics software (Version 20.0, Materialise NV, Leuven, Belgium) to process the STL files including duplications, translations, rotations, and nesting into labeled sinter boxes on the build platform. A PSW software (Version 3.6, EOS GmbH, Krailling, Germany) was used to slice the processed STL files with 100 μm layer thickness and send the sliced data to the Formiga P110 for a laser sintering using a 4 W laser scanning with a scanning speed of 1500–2000 mm/s.

A 3D bioplotter® manufacturer Series (EnvisionTEC, Gladbeck, Germany) system was used for extrusion-based 3D printing. 3D STL files of 3D constructs and grid pattern were imported into Perfactory RP® software suit and sliced into the layers with 200 μm thickness. Slicing data was then exported to the Visual Machine® plotting software on the 3D bioplotter to generate G-code instruction. Powder particles were loaded into a 10 mL stainless steel cartridge in a high temperature printing head and melted at 120C. After calibrating the printing head, a molten solution was extruded through a 400 μm nozzle by applying a pneumatic pressure of 9 bar (900 kPa) and the printing head moved along a pre-defined pathway at a velocity of

1.4 mm/s to create 3D constructs.

2.4 | Contact angle measurement

Contact angle on the surface of solid rectangular disks was measured using a Model 250 Standard Goniometer (Ramé-hart Instruments Co., NJ, USA). A 4 µL water drop was deposited using a micro-syringe on the top and side surfaces of rectangular constructs and contact angle of the drop against the surface was measured from an image of drop using DROPimage advanced software.

2.5 | In vitro degradation test

Solid and porous cylindrical constructs were immersed in individual tubes containing 15 mL of a 5 M sodium hydroxide (NaOH) solution to accelerate the hydrolytic degradation of the printed constructs.[15] The tubes were then incubated at 37C with gentle shaking for 1 month. Constructs removed from tubes at 1, 2, and 4 weeks after degradation were thoroughly washed with distilled water three times and dried at room temperature (RT) overnight for further analysis.

2.6 | Microscopy and scanning electron microscopy

The external morphology of the printed solid and porous constructs before and after degradation was observed using a Dino-lite digital microscope (AM3113T; AnMo Electronics Corp., Taiwan). In addition, the surface of the printed solid and porous constructs before and after degradation was observed using a Zeiss Ultra60 thermally assisted field emission scanning electron microscopy (FE-SEM; Carl Zeiss AG, Oberkochen, Germany) with an accelerating voltage of 4.0 kV.

2.7 | Mass loss measurement

Solid and porous constructs before and after degradation were weighed using a ME4002TE digital balance (Mettler-Toledo, USA). The mass loss (%) was calculated as (W_0 W_d)/W_0 100, where W_0 and W_d are the weights of the constructs before and after degradation, respectively.

2.8 | Mechanical test

Mechanical tests were performed using a 5944 Single Column mechanical testing system (Instron Corp., Norwood, MA, USA). Uniaxial compression was applied to solid and porous constructs at a constant velocity of 1 mm/min using a 2 kN load cell. The load and displacement measurements were recorded and then used to calculate the compressive modulus.

2.9 | µ-CT analysis

Microcomputed tomography (µ-CT) scanning was performed on the solid and porous constructs at a 36 µm voxel resolution using a Scanco µCT50 (Scanco Medical AG, Bassersdorf, Switzerland) with an X-ray source of 70 KVp at 200 µA. Mimics software (Version 23.0, Materialise NV, Leuven, Belgium) was used to create a 3D mask of the constructs using the Digital Imaging and Communications in Medicine (DICOM) files extracted from the scanned data. The Cavity Fill tool was used to fill the voids inside the solid constructs from the calculated polylines. The void fraction was then calculated as the percentage difference in volume between masks before and after applying Cavity Fill.

2.10 | Differential scanning calorimetry

Differential scanning calorimetry (DSC) was performed to analyze melting and crystallization behaviors using a Discovery Q250 with an RCS90 cooling system (TA instruments, New Castle, DE, USA). The dried solid and porous constructs were cut into the small pieces, weighted, and encapsulated in a Tzero® aluminum pan for DSC sample preparation. Samples were preheated to 120C at a rate of 20C/ min, followed by a 5 min isothermal hold to erase the thermal history. Samples were cooled to 0C and heated back up to 120C at a rate of 10C/min. Thermal transitions were then measured using the TA instruments TRIOS software.

2.11 | Gel permeation chromatography

Gel permeation chromatography (GPC) was performed using an Ecosec GPC autosampler (Tosoh Biosciences LLC, Montgomeryville, PA). The dried solid and porous constructs were cut into the small pieces, weighted, and fully dissolved in the chloroform with 0.25% (vol/vol) triethylamine. A volume of 1 mL of the solution was then filtered through 0.2 µm filter to remove HA. GPC analysis was performed at a flow rate of 0.450 mL/min, and weight average molecular weight (M_w) was calculated using Tosoh EcoSec Analysis software.

2.12 | Cell attachment and proliferation

Human bone marrow-derived mesenchymal stem cells (hMSCs) were purchased from Rooster Bio (MSC-003; Frederick, Maryland, USA). MSCs were cultured in low-glucose Dulbecco's modified Eagle's medium (DMEM, Gibco, USA) with 10% (vol/vol) fetal bovine serum (FBS, Gibco, USA) and 1% penicillin–streptomycin (Gibco, USA) at 37C in 5% CO_2 incubator with a humidified atmosphere. hMSCs were subcultured by four passages with medium change every 3 days. Confluent hMSCs were harvested using 0.05% (vol/vol) trypsin/EDTA solution (Gibco, USA), centrifuged at 1500 rev/min (rpm), and counted using an automated cell counter (Countess II FL, Thermo Fisher, Waltham, MA). The cell suspension with the determined number of

cells was transferred to a conical tube and centrifuged again. The supernatant medium was aspirated, and medium was added to obtain a cell suspension with 1.048 10^6/mL density.

The printed constructs were sterilized using 70% ethanol and dried overnight. The constructs were subsequently rinsed using sterile phosphate buffered saline (PBS) three times to remove the remaining ethanol and transferred into a 12-well tissue culture plate (Corning, NY, USA). A volume of 50 µL of cell suspension was dropped on the printed constructs and medium was gently added into a well after 90 min. The same amount of cell suspension was also dropped onto a well of 12-well plate to compare the initial cell attachment rate with the printed constructs. All cell/constructs were then cultured for 7 days and the cell attachment and proliferation of SLS- and extrusion-based constructs were evaluated using a Cell Counting Kit-8 (CCK-8, Dojindo Laboratory, Kumamoto, Japan) according to the manufacturer's instructions. Briefly, the hMSCs/constructs were washed using sterile PBS three times and incubated in a mixture of CCK-8 solution and medium (1:20, vol/vol) for 4 h at 37C in a humidified atmosphere of 5% CO_2. The optical density (OD) value of the conditioned media was then measured at 450 nm using a microplate reader (Biotek, USA).

2.13 | Cell viability

Viability of hMSCs on the printed constructs was evaluated at day 1 using LIVE/DEAD Viability/Cytotoxicity kit (Invitrogen, USA) according to the manufacturer's instructions. The hMSC/constructs were incubated in PBS containing calcein AM (1:1000, vol/vol) for staining live cells and ethidium homodimer (1:500, vol/vol) for staining dead cells at 37C for 15 min. The stained hMSCs were observed using a confocal microscope (Zeiss LSM 700B, Carl Zeiss, Germany) and taken images were processed using ZEN LE software (Carl Zeiss, Germany).

2.14 | Actin cytoskeleton/focal adhesion staining

The attachment of hMSCs on the printed constructs were evaluated by immunostaining at day 1 using Actin Cytoskeleton/Focal Adhesion Staining Kit (FAK100, MiliporeSigma, Burlington, MA, USA) and DAPI (Invitrogen, USA) according to the manufacturer's instructions. Briefly, the hMSCs/constructs were fixed using 4% paraformaldehyde for 15 min, permeabilized using 0.1% Triton X-100, and blocked using 1% bovine serum albumin (BSA) in PBS for 5 min at RT. After washing using a sterile PBS three times, the hMSCs/constructs were incubated in 1% BSA/PBS containing anti-Vinculin primary antibody (1:100, vol/vol) for 1 h and followed by incubation in 1% PBS containing TRITC-conjugated Phalloidin (1:250, vol/vol) for 30 min. The nucleus was counterstained with DAPI in PBS. The stained hMSCs were observed using a confocal microscope (Carl Zeiss, Germany) and taken images were processed using ZEN LE software (Carl Zeiss, Germany).

2.15 | Statistical analysis

Quantitative data were represented as the mean ± SD. Statistical analysis was performed using two-tailed Student's t test to determine significant difference between two experimental groups. A two-way analysis of variance with Tukey's post multiple comparisons test was performed for multiple experimental groups. Differences were considered to be statistically significant when p-value was less than .01. All of the experiments were performed more than three times.

3 | RESULTS

3.1 | 3D printed constructs

Porous and solid cylindrical constructs were successfully printed using both SLS- and extrusion-based 3D printing modalities. Porous constructs showed the same external geometries (Figure 1A,B).

However, SLS-based porous construct (S-PC) showed a rough morphology with a wider strut width than 500 µm while the extrusionbased porous construct (E-PC) had a high gloss surface with strut width as designed. In addition, SLS-based solid construct (S-SC) had a rough top surface without the trace of a laser beam path whereas the clear trace of the printing path was seen on the smooth top surface of extrusion-based solid construct (E-SC) (Figure 1C–F). The µCT scanning results showed significantly different printing results, including outer morphology and void fraction, between SLS-SC and E-SC (Figure 1G–J). The different surface roughness of the constructs printed using different 3D printing modalities also led the differences in the contact angle of water droplet on the surfaces (Figure 2K). The SLS-based construct was more hydrophobic, exhibiting a larger contact angle, compared to the extrusion-based construct. Interestingly, the contact angle of the water droplet decreased over time (5 min) on the surface of the SLS-based constructs while it remained unchanged on the surface of the extrusion-based constructs (data not shown).

3.2 | In vitro degradation behavior

3.2.1 | Morphological and mechanical characteristics change

The solid and porous constructs printed using both 3D printing modalities maintained the same outer geometries over the 4 weeks of degradation in NaOH; however, extrusion-based constructs showed more visible surface erosion by losing their glossy surfaces due to degradation (Figure 2A–D). Different rates of dimensional change and mass loss were also observed between two 3D printing modalities. The outer diameter had decreased more significantly in S-SC compared to the E-SC (Figure 2E). A more significant decrease of the strut width was also observed in S-PC compared

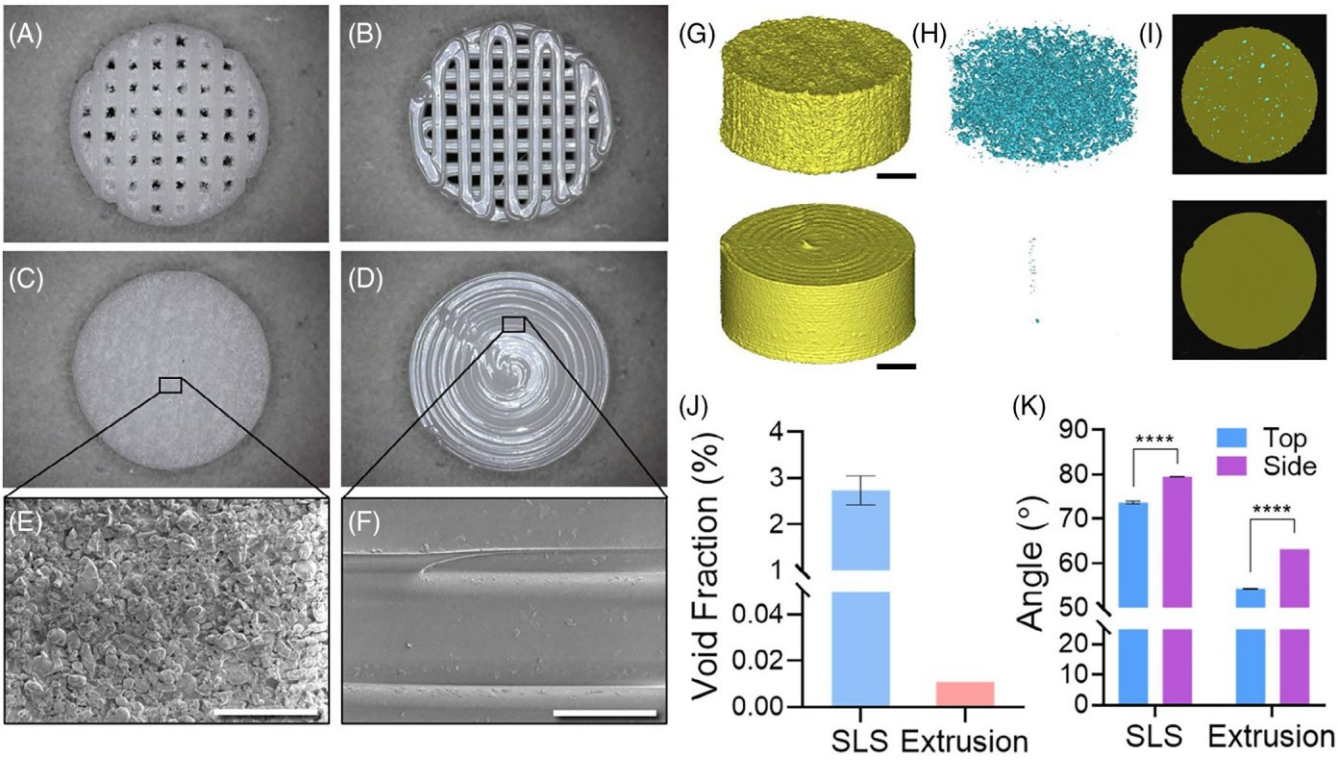

to E-PC (Figure 2F). The results of mass loss analysis showed that the SLS-based constructs had lost mass more significantly than the extrusion-based constructs (Figure 2G). The S-PC had the highest percentage weight loss among all constructs during the degradation. All printed constructs showed a similar trend in the compressive moduli during the degradation, with an initial increase followed by a subsequent decrease (Figure 2H).

The μ-CT scanning results showed a similar trend to the macroscopic observation results, with an obvious difference in the structural degradation behavior between two 3D printing modalities. The outer morphology of S-SC had maintained the same during the degradation; however, internal voids had gradually enlarged (Figure 3A). Cracks between the printed layers partially occurred at the outer side surface of the E-SC and had expanded inward during the degradation period (Figure 3B). A continuous decrease in the strut width of the S-PC was re-confirmed and the interval between the parallel struts had consequently increased (Figure 3C). Internal voids within the struts had also enlarged. In the case of the E-PC, the strut width had decreased slightly without the formation of internal voids within the struts (Figure 3D).

FIGURE 1 The 3D constructs printed using different 3D printing modalities. Top view of the porous construct printed using (A) SLS- and (B) extrusion-based 3D printing. Top view of the solid construct printed using (C) SLS- and (D) extrusion-based 3D printing. SEM image of the top surface of the solid construct printed using (E) SLS- and (F) extrusion-based 3D printing. White scale bar, 500 μm. (G) Constructed volume mask, (H) internal voids, and (I) cross-sectional area of the solid constructs printed using SLS (top) and extrusion 3D printing (bottom). Black scale bar, 2 mm. Comparison of (J) void fractions between cylindrical constructs and (K) contact angle of water droplet on the surfaces between the constructs printed using different 3D printing modalities (n = 5, ****p < .0001). SEM, scanning electron microscopy; SLS, selective laser sintering.

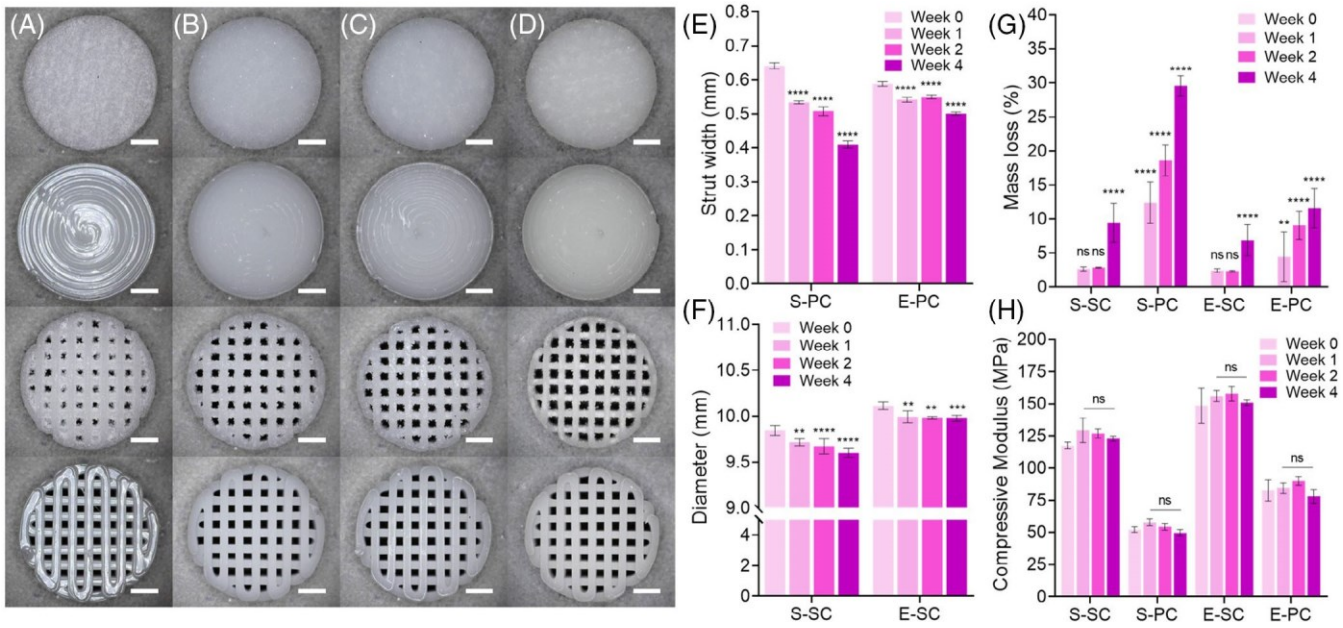

FIGURE 2 Photographs of the printed constructs at (A) 0, (B) 1, (C) 2, and (D) 4 weeks of degradation. White scale bar, 2 mm. All images show selective laser sintering (SLS)-based solid construct (S-SC), extrusion-based solid construct (E-SC), SLS-based porous construct (S-PC), and extrusion-based porous construct (E-PC) from top to bottom. Comparison of (E) diameter changes for the solid constructs, (F) strut width changes for the porous constructs (n = 5, **p < .01, ***p < .001, and ****p < .0001 vs. Week 0). Comparison of (G) mass loss and (H) compressive moduli changes for all constructs (n = 5, ns, not significant, **p < .01, and ****p < .0001 vs. Week 0).

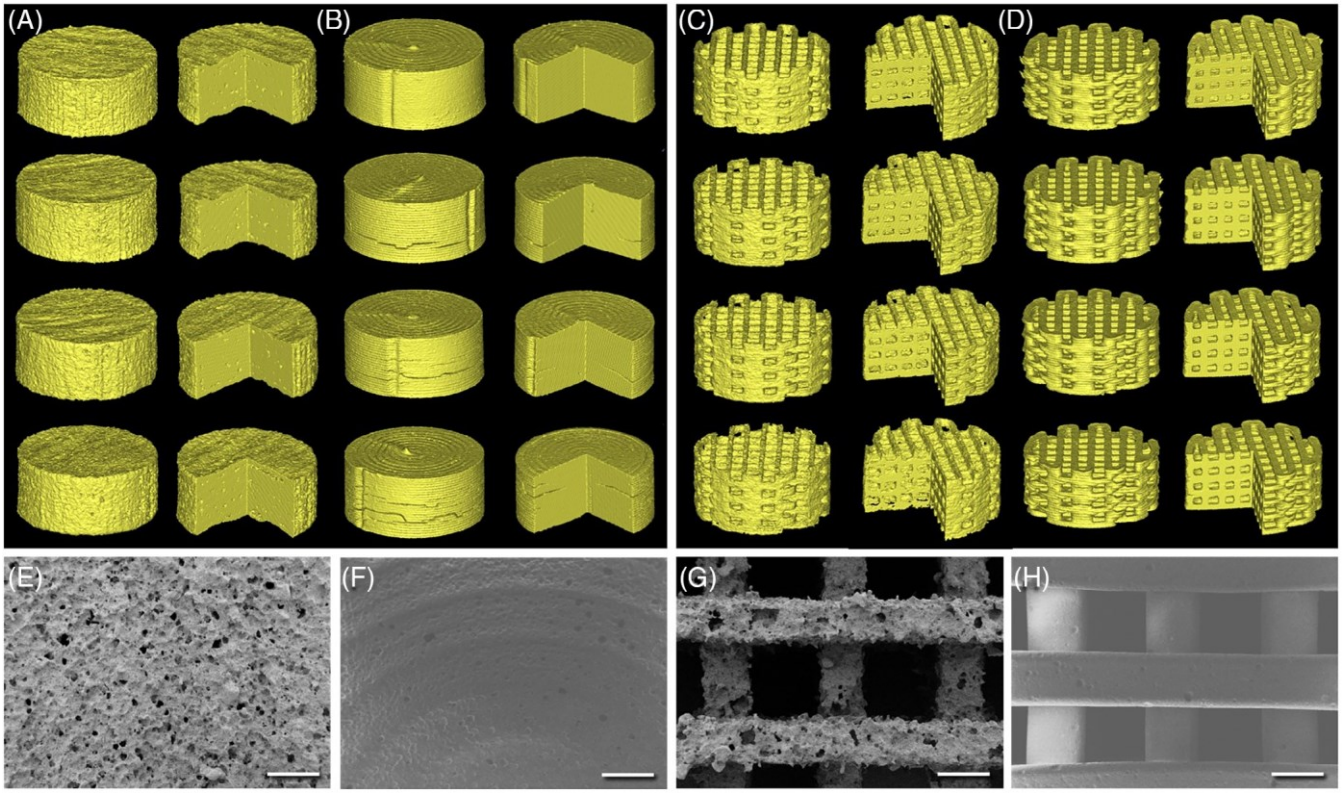

FIGURE 3 Constructed volume masks of (A) SLS-based solid construct (S-SC), (B) extrusion-based solid construct (E-SC), (C) SLS-based porous construct (S-PC), and (D) extrusion-based porous construct (E-PC). All images show the printed constructs at 0, 1, 2, and 4 weeks of degradation from top to bottom. SEM image of the top surface of (A) S-SC, (B) E-SC, (C) S-PC, and (D) E-PC at 4 weeks of degradation. White scale bar, 500 μm. SEM, scanning electron microscopy; SLS, selective laser sintering.

We also observed the surface of the constructs at 4 weeks of degradation. S-SC showed a rough surface morphology; however, the roughness was mitigated during degradation (Figure 3E). A large number of small holes, which are expected to be vacancies where HA particles have been released and enlarged due to degradation, were also observed. E-SC also had a large number of small holes, similar to those of S-SC, and the surface was quite different from before degradation due to the formation of wrinkles (Figure 3F). The surface of S-PC showed a similar trend to that of S-SC; however, additional cavities larger than small holes on the S-SC surface were also observed (Figure 3G). E-PC showed a quite similar trend on the strut surface to that of E-SC (Figure 3H).

3.2.2 | Material characteristics change

The M_w value of both solid and porous constructs printed using both 3D printing modalities were comparable before degradation (Figure 4A). A similar trend of a slight decrease in the M_w value in all constructs was observed throughout the degradation. All constructs also showed quite similar thermal properties, including crystallinity temperature, crystallinity enthalpy, melt temperature, and melt enthalpy, before degradation (Figure 4B–E). During the degradation period, a slight increase in the thermal properties was observed.

3.3 | Cell attachment and proliferation

The initial attachment rate of hMSCs on the printed constructs for both 3D printing modalities was much lower compared to that on tissue culture plates (TCP) (Figure 5A). The OD value for the extrusion-based constructs was slightly higher than that of the SLSbased constructs at day 1, which corresponds with the results of the contact angle measurement. A continuous increase in OD values was observed over 7 days for both 3D printing groups; however, cell proliferation was more significant in the extrusion-based constructs. At day 1, a number of dead cells were observed in the SLS-based constructs while no dead cells were detected in the extrusion-based constructs (Figure 5B,C). Furthermore, the MSCs attached on the printed constructs showed quite different morphologies depending on the 3D printing modalities. The hMSCs attached on the SLS-based constructs were spherical in appearance or partially spread (Figure 5D). However, the hMSCs were fully attached and spread out on the extrusion-based constructs (Figure 5E).

4 | DISCUSSION

Two representative 3D printing modalities used for producing clinical implants, SLS- and extrusion-based 3D printing, have different stem cells; SLS, selective laser sintering.

printing mechanisms and resulting characteristics. Each modality has its advantages and disadvantages. In SLS, a powder type material is exclusively used as the printing substrate. The thermal energy from the laser scanning on the powder layer induces viscous sintering, which forms a micro-melt layer at the surface of the powder particles and results in the aggregation of adjacent particles. SLS does not require additional support to hold the construct as the unsintered powder surrounds and supports the construct

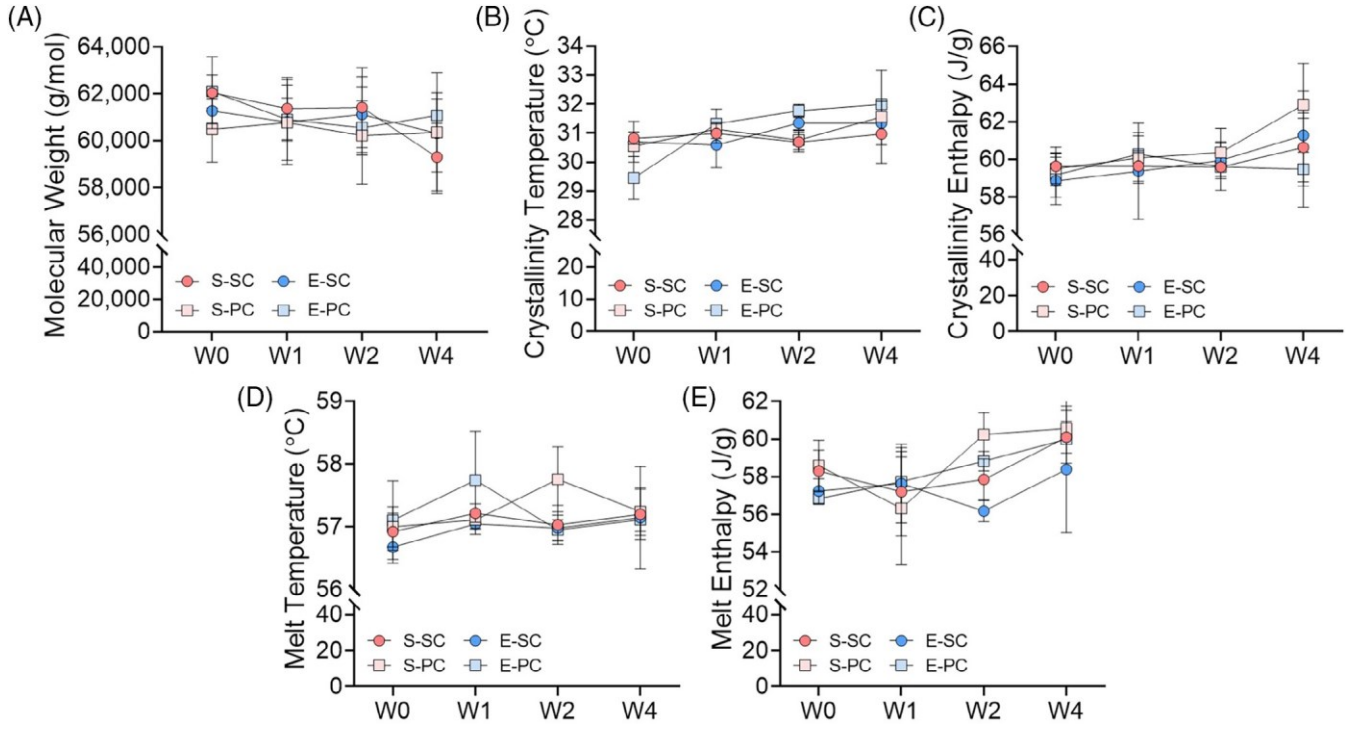

FIGURE 4 Comparison of (A) molecular weight, (B) crystallinity temperature, (C) crystallinity enthalpy, (D) melt temperature, and (E) melt enthalpy changes for all constructs. W0, W1, W2, and W4, indicate before degradation, 1, 2, and 4 weeks after degradation, respectively (n = 4).

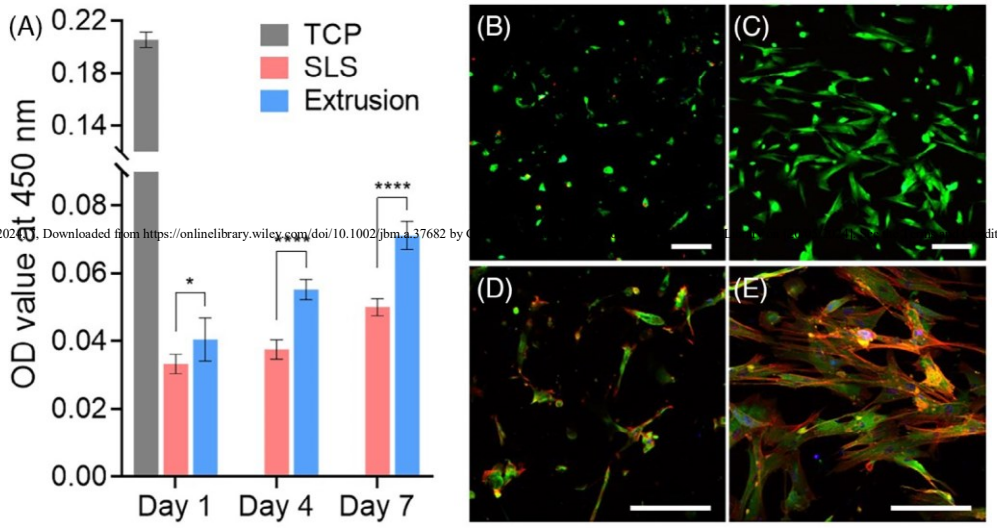

FIGURE 5 (A) Comparison of cell attachment and proliferation of SLS- and extrusion-based constructs (n = 5, *p < .05, and ****p < .0001). Live/dead staining images of the hMSCs attached on the (B) SLS- and (C) extrusion-based constructs at day 1 after cell seeding (green: live cells, red: dead cells). Scale bars, 200 μm. Actin Cytoskeleton/Focal Adhesion staining images of hMSCs attached on the (D) SLS- and (E) extrusionbased constructs at day 1 (red: F-actin, green: vinculin, and blue: nuclei). Scale bars, 200 μm. hMSCs, human bone marrow-derived mesenchymal

while it is being printed. This feature enables SLS to have a high level of design flexibility, allowing for the creation of intricate and complex 3D internal architectures, such as triply periodic minimal surfaces (TPMS), auxetics, and designs with overhangs, which can be challenging to achieve using extrusion-based 3D printing.[4,12,16,17]

In extrusion-based 3D printing, a layer is created by drawing the pattern using a strut extruded through a nozzle according to a pre-defined pathway. Although extrusion-based porous tissue engineering constructs have specific outer geometries that mimic the native tissues of interest, a typical grid pattern with continuous struts has been extensively used for the internal architecture.[14,18] This grid pattern is created by stacking multiple layers of parallel struts perpendicular to each other. Other patterns more complex than grids has been also used in extrusion-based 3D printing; however, most of them have been for tubular or 2D constructs.[19–22] A typical grid pattern was therefore used in this study to create constructs with a same geometry using both SLS- and extrusion-based 3D printing modalities.

In SLS-based 3D printing, a large amount of the powder is typically required for a single printing process to retain sufficient volume of the powder for proper laser penetration and sintering of the material. The quality of the powder, including its particle size distribution and level of dryness, is also crucial for successful SLS-based 3D printing. We have used a specific particle size range of 40–60 μm of cryogenically milled and sieved PCL powder which was mixed with 4% HA (wt/wt).[23] PCL serves as a printing substrate and HA serves as a flowing agent to improve powder distribution, forming a thin layer in the SLS process. Only this mixed PCL-HA powder was usable for SLSbased 3D printing used in this study. However, the relatively simple printing mechanism of extrusion-based 3D printing allows for a wide range of biomaterials to be used while SLS has limited material selectivity. Various biomaterials, including thermoplastic polymers and hydrogels, have been developed and engineered for use in extrusionbased 3D printing of tissue engineering constructs.[9,24,25] Multiple materials with small amounts can also be used by employing multiple printing heads that are independently controlled for printing each material to create a heterogeneous construct in a single extrusion-based 3D printing process while only a single powder-type material can be used in a single SLS process.[26] Although different types of PCL, pellet- or powder-type, even without HA can be used for extrusion-based 3D printing, the mixed PCL-HA powder that can be usable for SLS was used for both 3D printing modalities.

The implementation of different 3D printing modalities for the same biomaterial led to distinct differences in the printing outcomes, including mechanical properties, degradation rate, and cell responses of the printed constructs. The rough morphologies of SLS-based constructs, including rough surfaces and internal void fractions, was attributed to the inherent printing mechanism of SLS, aggregation of the powder particles.[7] The same powder material was used for extrusion-based 3D printing; however, it was completely melted into the solution state and extruded as a solid strut through a nozzle, creating the constructs with a smooth surface and void fraction closed to zero. Unexpected air bubbles in the molten solution and tiny gap between the printed parallel struts rarely increased the void fraction of the extrusion-based constructs. It was obvious that extrusionbased constructs were stiffer than SLS-based constructs, which had a much higher void fraction.

Regardless of 3D printing modality used, the printed constructs underwent homogeneous degradation by surface erosion during hydrolytic degradation using a NaOH solution.[15,27,28] It has been reported that PCL has a sustained degradation period due to its highmolecular weight and the slow diffusion rate resulting from its inherent hydrophobicity.[28] However, the SLS-based constructs showed a higher degradation rate than the extrusion-based constructs due to their rough morphologies, including rough surfaces and internal void fractions. The rough surface of the SLS-based constructs resulted in a larger external surface area, accelerating surface erosion. In addition, internal voids of the SLS-based constructs increased the diffusion rate of the NaOH solution into the constructs, and the degradation of the SLS-based constructs was further accelerated by internal voids located close to the surface, which were exposed due to surface erosion during the degradation process. Both large surface area and interval voids of SLS-based constructs contributed to the significant decrease in dimensions, such as outer diameter of S-SC and strut width of S-PC, as well as mass loss compared to the extrusion-based constructs.

The formation of a rough morphology, including internal void fraction, is an inherent characteristic of SLS-based 3D printing. It has been reported that this characteristic can possibly impair the mechanical stability of the SLS-based 3D scaffold or implant, raising the potential risk of unexpected failure under complex in vivo environments.[12,29,30] However, in vitro degradation test results revealed that extrusion-based constructs also have an issue in terms of mechanical stability, with cracks developing between the printed layers during degradation. This could potentially lead to structural failure when the constructs are subjected to external loads applied perpendicular to the stacking direction. Therefore, the interlayer adhesion and the stacking direction (printing orientation) is more crucial in extrusion-based 3D printing compared to the SLS-based 3D printing.[10,31]

Different 3D printing modalities did not influence the material properties of the biomaterial used. All of the printed solid and porous constructs not only showed similar material properties including molecular weight and thermal properties, but also exhibited a similar trend of material property changes during the degradation. The compression test results confirmed that the increase of thermal properties, including crystallinity, led to the slight increase in compressive moduli of all constructs at the early stage of the degradation.[32] However, the substantial decrease in the compressive moduli despite the continuous decrease in thermal properties at the later stage of the degradation was primarily attributed to the significant decrease in their outer dimensions. The enzymatic degradation, which takes place during the later stage of the degradation and causes significant material property changes, was not observed within 4 weeks of the degradation.[27]

The distinct surface morphologies of SLS- and extrusion-based constructs led to different cell responses, including cell attachment rate, morphology, and proliferation. The SLS-based constructs with a rough

surface showed a relatively poor cell attachment rate compared to the extrusion-based constructs with a smooth surface. The difference in the cell attachment rate between SLS- and extrusionbased constructs led to the difference in cell proliferation. The initial poor cell attachment rate of the SLS-based constructs was attributed to unstable cell-substrate contacts.[33] The round or partial spread of the cells attached on the SLS-based constructs were also associated with this unstable cell-substrate contracts resulting from the rough surface morphology. In contrast, the attached cells on the extrusion-based constructs with a smooth surface were observed to spread out completely. Although in vitro cell responses were more significant in the extrusion-based constructs compared to the SLSbased constructs, the difference between the two 3D printing modalities was not substantial. The cell attachment rate of the extrusion-based constructs was still significantly lower than that of TCP, due to the inherent hydrophobicity of PCL. Meanwhile, the rough morphology of the SLS-based tissue scaffolds has also been reported to support cell attachment and tissue infiltration in vivo.[34,35] In those regards, future work will include further comparison of two 3D printing modalities in terms of their in vivo performance, including tissue regeneration capacity and tissue-implant interaction.

5 | CONCLUSION

A direct and comprehensive comparison of SLS- and extrusion-based 3D printing modalities was performed in this study. Implementation of different modalities for 3D printing of the same biomaterial led to distinct differences in the printing outcomes. Extrusion-based 3D printing resulted in the constructs with a low internal void fraction and a smooth surface morphology compared to those printed using SLS. These characteristics led to increased stiffness, higher cell attachment and proliferation rates, and a delayed degradation rate for the printed constructs. Given that each 3D printing modality has inherent characteristics and consequential distinct printing outcomes, 3D printing modality is another critical consideration for biomedical and tissue engineering applications.

AUTHOR CONTRIBUTIONS

J.H.P.: Designed research. J.H.P., S.J.T, J.-K.Y.: Performed research. J.H.P., Y.K., S.J.H.: Supervised the research. J.H.P.: Analyzed the data and wrote the manuscript. All authors discussed and reviewed the manuscript.

ACKNOWLEDGMENT

This research was supported by US National Institutes of Health (NIH) (R01 HD 086201) and NSF grant 2314241 Partnership for Innovation Grant "Resorb3D: A 3D Printed Resorbable Bio-Tissue Platform for Craniofacial Implant".

CONFLICT OF INTEREST STATEMENT

The authors declare no conflict of interest.

DATA AVAILABILITY STATEMENT

The data that support the findings of this study are available from the corresponding author upon reasonable request.

ORCID

Jeong Hun Park https://orcid.org/0000-0001-7408-4460

REFERENCES

1. Han HH, Shim J-H, Lee H, et al. Reconstruction of complex maxillary defects using patient-specific 3D-printed biodegradable scaffolds. Plast Reconstr Surg Glob Open. 2018;6(11).
2. Zopf DA, Hollister SJ, Nelson ME, Ohye RG, Green GE. Bioresorbable airway splint created with a three-dimensional printer. N Engl J Med. 2013;368(21):2043-2045.
3. Saito E, Liu Y, Migneco F, Hollister SJ. Strut size and surface area effects on long-term in vivo degradation in computer designed poly (L-lactic acid) three-dimensional porous scaffolds. Acta Biomater. 2012;8(7):2568-2577.
4. Zhou M, Hou J, Zhang G, et al. Tuning the mechanics of 3D-printed scaffolds by crystal lattice-like structural design for breast tissue engineering. Biofabrication. 2019;12(1):015023.
5. Daly AC, Kelly DJ. Biofabrication of spatially organised tissues by directing the growth of cellular spheroids within 3D printed polymeric microchambers. Biomaterials. 2019;197:194-206.
6. Shim J-H, Lee J-S, Kim JY, Cho D-W. Bioprinting of a mechanically enhanced three-dimensional dual cell-laden construct for osteochondral tissue engineering using a multi-head tissue/organ building system. J Micromech Microeng. 2012;22(8):085014.
7. Partee B, Hollister SJ, Das S. Selective laser sintering process optimization for layered manufacturing of CAPA® 6501 polycaprolactone bone tissue engineering scaffolds. J Manuf Sci Eng. 2006;128: 531-540.
8. Billiet T, Gevaert E, De Schryver T, Cornelissen M, Dubruel P. The 3D printing of gelatin methacrylamide cell-laden tissue-engineered constructs with high cell viability. Biomaterials. 2014;35(1):49-62.
9. Kim H, Kang B, Cui X, et al. Light-activated decellularized extracellular matrix-based bioinks for volumetric tissue analogs at the centimeter scale. Adv Funct Mater. 2021;31(32):2011252.
10. Ding S, Zou B, Wang P, Ding H. Effects of nozzle temperature and building orientation on mechanical properties and microstructure of PEEK and PEI printed by 3D-FDM. Polym Test. 2019;78:105948.
11. Do AV, Khorsand B, Geary SM, Salem AK. 3D printing of scaffolds for tissue regeneration applications. Adv Healthc Mater. 2015;4(12): 1742-1762.
12. Kelly CN, Miller AT, Hollister SJ, Guldberg RE, Gall K. Design and structure–function characterization of 3D printed synthetic porous biomaterials for tissue engineering. Adv Healthc Mater. 2018;7(7): 1701095.
13. Mota C, Puppi D, Chiellini F, Chiellini E. Additive manufacturing techniques for the production of tissue engineering constructs. J Tissue Eng Regen Med. 2015;9(3):174-190.
14. Kang H-W, Lee SJ, Ko IK, Kengla C, Yoo JJ, Atala A. A 3D bioprinting system to produce human-scale tissue constructs with structural integrity. Nat Biotechnol. 2016;34(3):312-319.
15. Lam CX, Teoh SH, Hutmacher DW. Comparison of the degradation of polycaprolactone and polycaprolactone–(β-tricalcium phosphate) scaffolds in alkaline medium. Polym Int. 2007;56(6):718-728.

16. Coelho PG, Hollister SJ, Flanagan CL, Fernandes PR. Bioresorbable scaffolds for bone tissue engineering: optimal design, fabrication, mechanical testing and scale-size effects analysis. Med Eng Phys. 2015;37(3):287-296.

17. Meng Z, He J, Li D. Additive manufacturing and large deformation responses

28. Yeo A, Sju E, Rai B, Teoh SH. Customizing the degradation and load-bearing profile of 3D polycaprolactone-tricalcium phosphate scaffolds under enzymatic and hydrolytic conditions. J Biomed Mater Res Part B: Appl Biomater. 2008;87(2):562-569.
29. Meng Z, He J, Cai Z, et al. In-situ re-melting and re-solidification treatment of selective laser sintered polycaprolactone lattice scaffolds for improved filament quality and mechanical properties.Biofabrication. 2020;12(3):035012.
30. Song P, Hu C, Pei X, et al. Dual modulation of crystallinity and macro-/microstructures of 3D printed porous titanium implants to enhance stability and osseointegration.J Mater Chem B. 2019;7(17):2865-2877.
31. Andreu A, Kim S, Dittus J, Friedmann M, Fleischer J, Yoon Y-J. Hybrid material extrusion 3D printing to strengthen interlayer adhesion through hot rolling. Addit Manuf. 2022;55:102773.
32. Atwood JL. Comprehensive Supramolecular Chemistry II. Elsevier; 2017.
33. Wang PY, Clements LR, Thissen H, Jane A, Tsai WB, Voelcker NH. Screening mesenchymal stem cell attachment and differentiation on porous silicon gradients. Adv Funct Mater. 2012;22(16):3414-3423.
34. Du Y, Liu H, Yang Q, et al. Selective laser sintering scaffold with hierarchical architecture and gradient composition for osteochondral repair in rabbits. Biomaterials. 2017;137:37-48.
35. Yeong W, Sudarmadji N, Yu H, et al. Porous polycaprolactone scaffold for cardiac tissue engineering fabricated by selective laser sintering. Acta Biomater. 2010;6(6):2028-2034.

How to cite this article: Park JH, Tucker SJ, Yoon J-K, Kim Y, Hollister SJ. 3D printing modality effect: Distinct printing outcomes dependent on selective laser sintering (SLS) and melt extrusion. J Biomed Mater Res. 2024;112(7):1015-1024. doi:10.1002/jbm.a.37682

of highly-porous polycaprolactone scaffolds with helical architectures for breast tissue engineering. Virtual Phys Prototyp. 2021;16(3):291-305.

18. Shim J-H, Jang K-M, Hahn SK, et al. Three-dimensional bioprinting of multilayered constructs containing human mesenchymal stromal cells for osteochondral tissue regeneration in the rabbit knee joint. Biofabrication. 2016;8(1):014102.
19. Brazhkina O, Park JH, Park H-J, et al. Designing a 3D printing based auxetic cardiac patch with hiPSC-CMs for heart repair. J Cardiovasc Dev Dis. 2021;8(12):172.
20. Ha D-H, Chae S, Lee JY, et al. Therapeutic effect of decellularized extracellular matrix-based hydrogel for radiation esophagitis by 3D printed esophageal stent. Biomaterials. 2021;266:120477.
21. Ha D-H, Kim JY, Park TS, et al. Development of a radiopaque, longterm drug eluting bioresorbable stent for the femoral-iliac artery. RSC Adv. 2019;9(59):34636-34641.
22. Park JH, Ahn M, Park SH, et al. 3D bioprinting of a trachea-mimetic cellular construct of a clinically relevant size. Biomaterials. 2021;279: 121246.
23. Zopf DA, Flanagan CL, Wheeler M, Hollister SJ, Green GE. Treatment of severe porcine tracheomalacia with a 3-dimensionally printed, bioresorbable, external airway splint. JAMA Otolaryngol—Head Neck Surg. 2014;140(1):66-71.
24. Pati F, Jang J, Ha D-H, et al. Printing three-dimensional tissue analogues with decellularized extracellular matrix bioink. Nat Commun. 2014;5(1):3935.
25. Yan M, Awad H. Optimizing rheological properties for printability: low-temperature extrusion 3D printing of hydroxyapatitepolycaprolactone mixture inks for bone tissue engineering. Front Mater. 2023;10:1239692.
26. Jung JW, Lee J-S, Cho D-W. Computer-aided multiple-head 3D printing system for printing of heterogeneous organ/tissue constructs. Sci Rep. 2016;6(1):21685.
27. Lam CX, Savalani MM, Teoh S-H, Hutmacher DW. Dynamics of in vitro polymer degradation of polycaprolactone-based scaffolds: accelerated versus simulated physiological conditions. Biomed Mater. 2008;3(3):034108.